

CONSTRAINING THE HIGH DENSITY NUCLEAR SYMMETRY ENERGY WITH PIONS

By

Justin Estee

A DISSERTATION

Submitted
to Michigan State University
in partial fulfillment of the requirements
for the degree of

Physics – Doctor of Philosophy

2019

ABSTRACT

CONSTRAINING THE HIGH DENSITY NUCLEAR SYMMETRY ENERGY WITH PIONS

By

Justin Estee

Copyright by
JUSTIN ESTEE
2019

ACKNOWLEDGEMENTS

Your acknowledgements here.

TABLE OF CONTENTS

LIST OF TABLES	vii
LIST OF FIGURES	viii
CHAPTER 1 INTRODUCTION	1
1.1 From Nuclear Forces to the Equation of State	1
1.2 Phases of Nuclear Matter	1
1.3 The Nuclear Equation of State	1
1.4 Boltzmann Ulong Uhlenbeck (BUU) Transport Code	1
1.5 Observables	1
1.6 The π observable	1
1.7 Previous Constraints	1
1.8 Motivation for building the S π RIT TPC	2
CHAPTER 2 THEORY	3
CHAPTER 3 EXPERIMENT	4
3.1 S π RIT TPC Overview	4
3.1.1 Enclosure	5
3.1.2 Voltage Step Down	5
3.1.3 Field Cage	5
3.1.4 Voltage Step Down	7
3.1.5 Wire Planes	7
3.1.6 Pad Plane	7
3.1.7 Electronics	7
3.1.8 Considerations when constructing a TPC	8
3.1.9 Gas Properties	8
3.2 Ancillary Detectors	10
3.2.1 Kyoto Multiplicity Trigger	10
3.2.2 Krakow ?????? (KATANA)	10
3.3 Radio Isotope Beam Factory (RIBF) Facility	10
3.4 S π RIT at RIBF	11
3.5 Experimental Setup	11
3.6 Trigger Condition	11
3.7 Collision Data Taken	12
CHAPTER 4 DATA ANALYSIS I: CALIBRATION AND CORRECTIONS	13
4.1 Software	13
4.2 Calibrations and Corrections	16
4.2.1 Cocktail calibration	16
4.2.2 Electronics calibration	16
4.2.3 Anode gain calibration	18

4.2.4	Extending the dynamic range of the Electronics	18
4.2.5	Space Charge Corrections	19
4.3	Monte Carlo Simulation	28
4.3.1	Drift Task	29
4.3.2	Pad Response Task	29
4.3.3	Electronics Task	30
4.3.4	Simulating Saturation	31
4.4	Monte Carlo Track Embedding	31
4.4.1	MC and Data Comparison	32
4.5	Efficiency Corrections	33
4.6	Beam Particle Identification	33
4.7	Solid angle coverage	33
CHAPTER 5 DATA ANALYSIS II: EXTRACTING PHYSICS		29
5.1	Impact Parameter Selection	29
5.2	Track Quality Cuts	29
5.3	Angular Quality Cuts	29
CHAPTER 6 RESULTS		22
6.1	Comparison to Theory	22
6.2	π Yields	22
6.3	π^-/π^+ Ratio	22
6.4	Pion Inferometry	22
6.5	Constraint on the Symmetry Energy	22
APPENDIX		23
BIBLIOGRAPHY		25

LIST OF TABLES

Table 3.1	An overview of the properties of the S π RIT TPC	5
Table 3.2	Summary of range of GET electronics settings.	8
Table 3.3	9
Table 4.1	Summary of expected cocktail.	17
Table 4.2	Average energy loss of each beam.	26

LIST OF FIGURES

Figure 3.1	Exploded view of the S π RIT TPC	6
Figure 3.2	Drift velocity of electrons in P10 gas.	9
Figure 3.3	Number of electrons produced in a single avalanche on an anode wire. Two different voltages were simulated using Garfield++ at 1470 V and 1214 V. The expected Polya distribution fit is also given in yellow.	10
Figure 3.4	Overview of the RIBF, BigRIPS, and SAMURAI beamline.	11
Figure 4.1	Cartoon graphic of a top down view of a fit to a track passing through several pads. The bolded pads and the charges q_i represent the hits belonging to that pad and the clusters of the track representing the average position of the track. The three clusters at the bottom are clustered in the x-direction and for the upper three clustered in the z-direction. The estimate of the position of the avalanche is given by the track fit and the position from the center to each pad to the \bar{x} position is given as λ_i	15
Figure 4.2	A cartoon illustration of the charge distribution resulting from an electron avalanche on one wire and the projections of the distribution onto the two axis $\rho(x)$ onto the x-axis and $\rho(z)$ onto the z-axis. The orientation of the wire planes is flipped upside down to display the perspective better.	16
Figure 4.3	Calibration of electronics	17
Figure 4.4	Calibration of low high.	18
Figure 4.5	Location of space charge in ^{132}Sn	19
Figure 4.6	Beam path of the experiments	20
Figure 4.7	ΔV_x distribution for left-going and right-going tracks in the TPC for the	22
Figure 4.8	ΔV_{LR} as a function of the beam rate.	23
Figure 4.9	Space charge relation	24
Figure 4.10	Shift of tracks	25
Figure 4.13	A summary of all the effects modeled in the TPC MC simulation.	29
Figure 4.14	A cartoon of the wires over one pad.	30
Figure 4.15	Comparison of MC and data PRF	30

Figure 4.16 Pulse shapes for normal and saturated signals. Both are normalized to a max height of 1.	31
--	----

CHAPTER 3

EXPERIMENT

3.1 S π RIT TPC Overview

Add Overview image with labels

The Samurai Pion-Reconstruction and Ion Tracker Time Projection Chamber (S π RI TPC) is a Multi-Wire Proportional Counter developed to measure pions and other light charge particles resulting from radioactive heavy ion collisions in a fixed target experiments. The TPC is enclosed in a thin aluminum sheet walls all around in order to minimize neutron scattering and to allow for light charged particles to reach the arrays of scintillating bars detectors on the sides and downstream of the TPC. The S π RI TPC was developed to fit inside the Samurai dipole magnet used at the Rare Isotope Beam Factory (RIBF) at RIKEN in Wako-shi, Japan [1]; the dipole gap limited the vertical space of the TPC. More detail and specifications of the Samurai dipole magnet are given in [2].

A target ladder allowed for up to 5 fixed targets to be mounted. A ACME worm gear allowed for the x-axis motion for changing the targets during the experiment, without needing to open or move the TPC. The motion of this worm gear was translated through the target motion feed-through by several brass gears and non-magnetic gear boxes. The motion of the target ladder could be controlled by hand or by operation of the drill. The targets were mounted on stand-offs on the target ladder and also had z-axis motion. This allowed for the targets to be positioned as close as possible to the thin window of the field cage, maximizing the geometric acceptance.

The electronics were mounted to the aluminum top plate. Several aluminum ribs were mounted to the top of the plate to bring structural rigidity. A flatness within $150\mu\text{m}$ was achieved across the whole top plate as measured by a laser position system. The charge sensitive pads of the pad plane were etched into several circuit boards were recessed and glued to the bottom portion of the top plate. Vias through the pad plane circuit boards brought the signal traces from the pads to surface mount pads on the other side of the boards. Several holes cut through the top plate allowed for the

S π RIT TPC Overview	
Pad plane area	1.3 m x .9 m
Pad size	1.2 cm x .8 cm
Number of pads	12096 (112 x 108)
Gas composition	90% Ar + 10% CH ₄
Multiplicity limit	200
dE/dx range	Z=1-8, π , p,d,t,He,Li-O
Drift length	50 cm

Table 3.1: An overview of the properties of the S π RIT TPC

interface cables of the electronics to be connected to these surface pads.

Just below the pad plane were a set of three wire planes; the gating grid, ground, and anode wire planes. The detailed function of these wires will be explained later but they served to separate the boundary between the drift volume and the avalanche volume.

The front and sides of the field cage were assembled from 8 independent rigid circuit boards. The downstream window served as the downstream wall of the field cage all though it was was a large polycarbonate frame in which a removable kapton window could be installed. This thin window minimized the scattering of exiting neutrons and charged particles for downstream detectors.

The voltage step down takes the high voltage of the field cage cathode and steps the voltage down through a set of copper rings and a resistor chain, minimizing the chance for sparking.

3.1.1 Enclosure

3.1.2 Voltage Step Down

3.1.3 Field Cage

The field cage was designed to hang from the top plate and therefore needed to be of a lightweight construction. Also the materials needed to be thin to allow for light charged particle and neutrons to pass through without significant scattering for ancillary detectors. Therefore instead of a

downstream wall, a large thin exit window was constructed. The cathode was constructed of an aluminum honeycomb laminate. Two sheets of ??? aluminum were bonded to a core of aluminum honeycomb structure providing a lightweight yet rigid structure for the cathode.

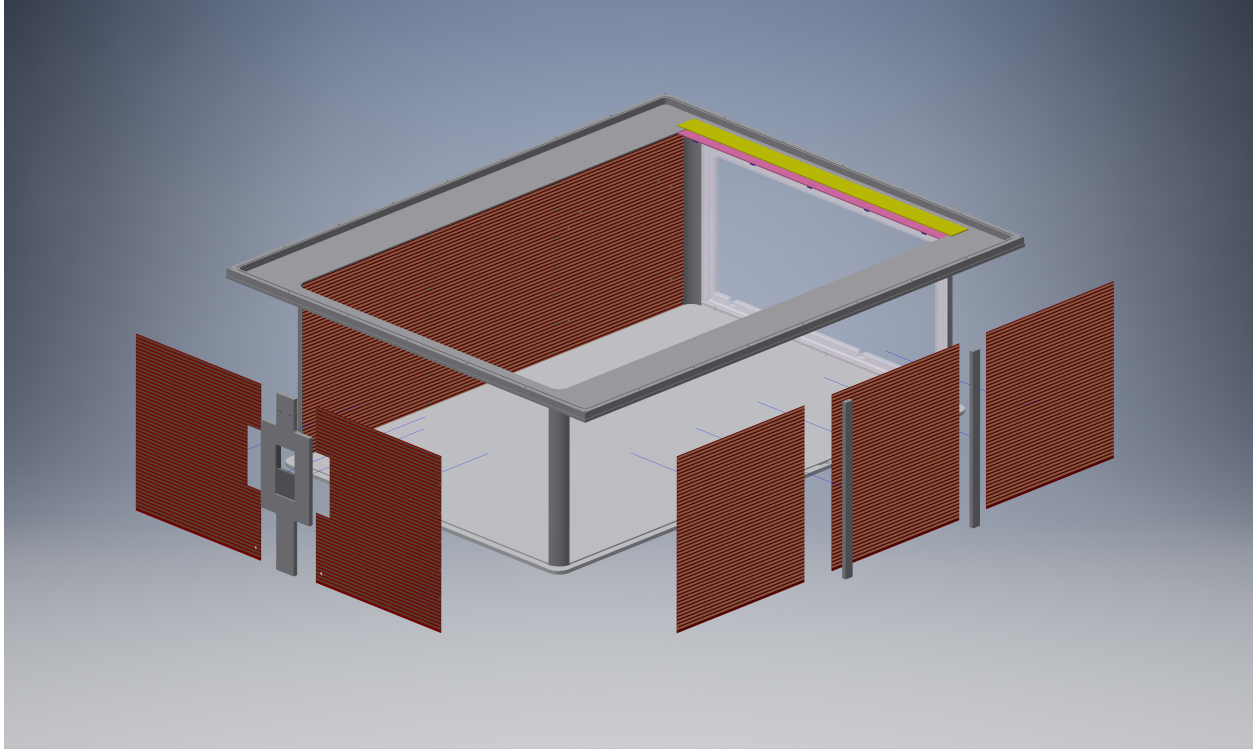


Figure 3.1: Exploded view of the $S\pi$ RIT TPC

The field cage was constructed from several panels of printed circuit boards (PCBs). The epoxy in the common PCB substrate FR4 contains bromine which is not suitable for the long term operation of a TPC, as the bromine will eventually cause gain reduction of the wires [CITE]. The halogen free material chosen was Rogers ???. We built the TPC with the option to run explosive gases such as hydrogen, thus we decided to have field cage an isolated volume from the rest of the TPC enclosure. While the risk of a high voltage spark was minimized using the voltage step down, the risk of sparking when using an explosive gas could be further minimized by isolating the detector volume from the enclosure volume thereby allowing you to run an insulating gas between the field cage while running the explosive gas inside the detector volume only.

The front of the field cage was made of two PCBs and each side was constructed of three PCBs.

The exit window was a $10\mu\text{m}$ thick Kapton window with evaporated aluminum strips on the inside and outside; mounted on a polycarbonate frame.

3.1.4 Voltage Step Down

To lower the risk of a high voltage spark around the cathode region a voltage step down was developed. A series of 7 concentric copper rings with 20 MOhm resistors between them steps the cathode voltage down to ground. This minimizes sharp transitions of the electric field and therefore sparking.

3.1.5 Wire Planes

Add figure of gating grid transparency closed and open configuration

3.1.6 Pad Plane

Add figure of close up of pad plane

3.1.7 Electronics

Signals in the $S\pi\text{RIT}$ TPC are amplified and digitized by the recently developed Generic Electronics for TPCs (GET) [3]. Short cables transmit the signals from the pads to the inputs of the AGET chips. Each AGET chip services 64 pads (63 pads are connected in our case), contains a pre-amplifier, and a Switched Capacitor Array (SCA), with a maximum of 512 time buckets with an adjustable sampling frequency of 1 to 100 MHz. Four AGET chips are mounted on one AsAd (ASIC and ADC) motherboard. The gain of each AGET can be configured as 0.12, 0.24, 1.0, or 10 pC over the whole dynamic range, and the ADCs on each AsAd board provides 12 bit resolution. The peaking times of the shaping amplifiers can be set to 69, 117, 232, 501, 720, or 1014 ns. In this experiment, the gain was set to the highest setting, 0.12 pC, the peaking time 117 ns, and the sampling frequency 25 MHz (resulting in 40 ns time buckets). The Aget 2.0, asad 2.1, and cobo 1.0 firmware versions

GET electronics settings	
ADC bit range	14 bits
Sampling frequency	1-100 MHz
Dynamic range	.12, .24, 1.0, 10pC
Peaking time	69,117,232,501,720,1014 ns
Time bucket range	512

Table 3.2: Summary of range of GET electronics settings.

were used. The variations in the electronics were calibrated by measuring the response of each channel to a injected reference pulse, covering the full dynamic range of each channel.

3.1.8 Considerations when constructing a TPC

Several considerations went into the construction of the $S\pi$ RI TPC which I wish to summarize and document here. All materials and glues of the TPC were selected as low out-gassing materials. Several materials (that are common place in nuclear labs), such as vacuum grease, viton o-rings, all out-gas organic chemicals into the counter gas which damage the TPC by permanently lowering the gain over time. The organic molecules responsible are difficult to identify exactly, but lists of good and bad materials are well known in the literature from experiments. If a material we wished to used was not on these lists we placed the material in a clean chamber with the counter gas and flowed this counter gas through a small proportional counter making sure the gain did not drop at high collection rates when exposed to a high rate alpha Americium source.

Sparking Two volumes of gas.

3.1.9 Gas Properties

$$\frac{d\vec{x}}{dt} = \frac{\mu}{1 + (\omega\tau)^2} \left(\vec{E} + \omega\tau \frac{\vec{E} \times \vec{B}}{|\vec{B}|} + \omega^2\tau^2 \frac{\vec{E} \cdot \vec{B}}{|\vec{B}|^2} \vec{B} \right) \quad (3.1)$$

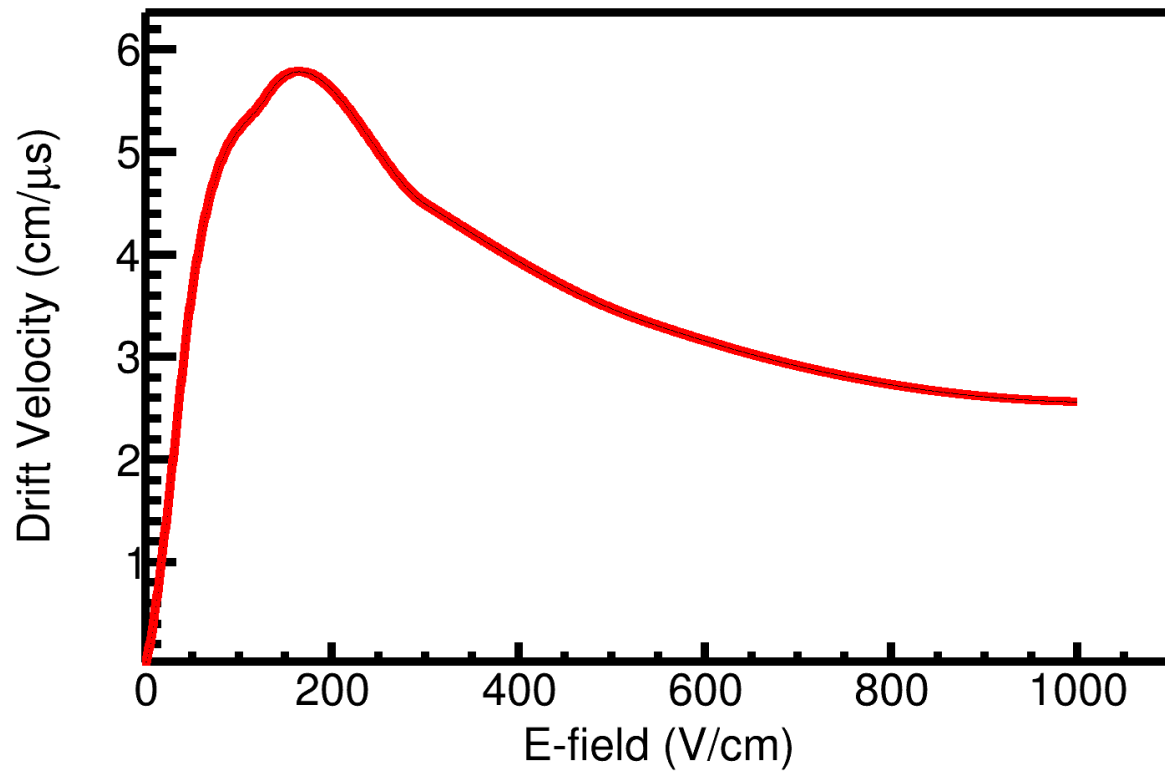


Figure 3.2: Drift velocity of electrons in P10 gas.

Gas properties	σ_t ($\text{cm}^{-1/2}$)	σ_l ($\text{cm}^{-1/2}$)	v_d ($\text{cm } \mu\text{s}^{-1}$)	v_i ($\text{cm } \mu\text{s}^{-1}$)	G_h	G_l
	0.024	0.034	5.43	2.05×10^{-4}	903	150

Table 3.3

Add table for gas diffusion

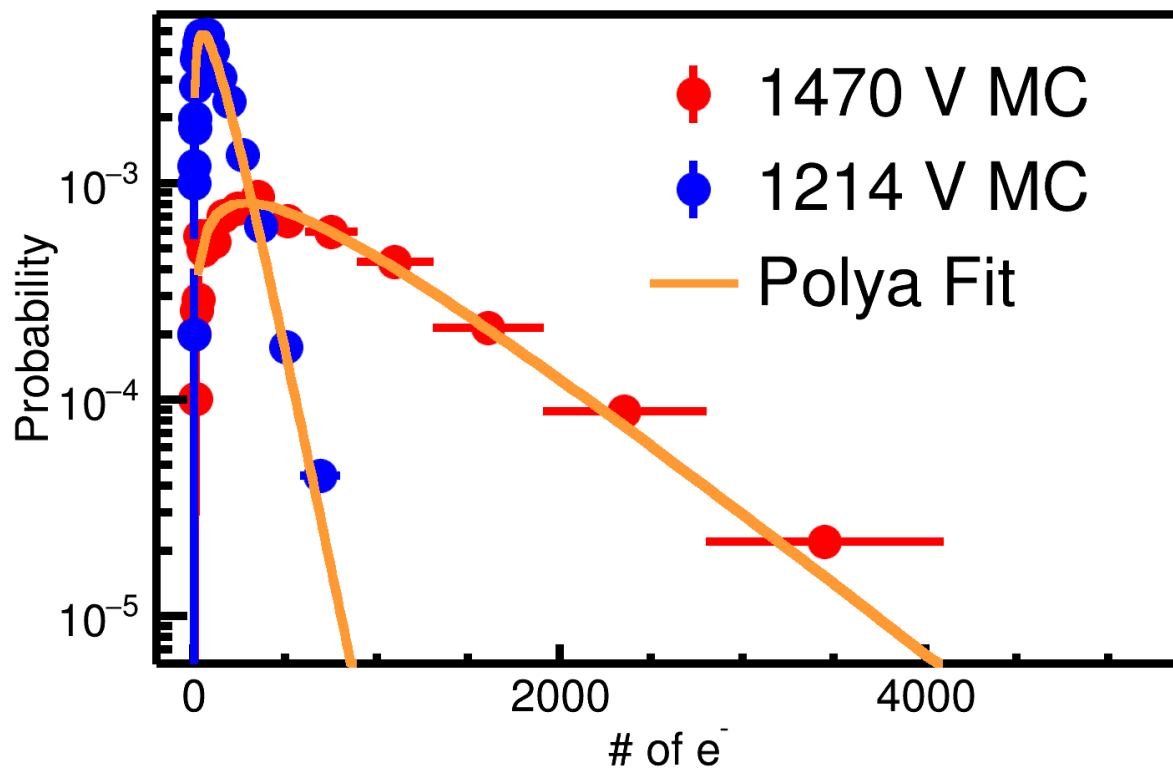


Figure 3.3: Number of electrons produced in a single avalanche on an anode wire. Two different voltages were simulated using Garfield++ at 1470 V and 1214 V. The expected Polya distribution fit is also given in yellow.

3.2 Ancillary Detectors

3.2.1 Kyoto Multiplicity Trigger

3.2.2 Krakow ?????? (KATANA)

3.3 Radio Isotope Beam Factory (RIBF) Facility

Cyclotron facility overview. Samurai line overview. Beam line element overview. Big ribs beam PID. reference

3.4 $S\pi$ RIT at RIBF

Picture of setup.

SAMURAI (Superconducting Analyzer for Multi-particles from Radioisotope beams) is a large-acceptance multi-particle spectrometer for radioactive-beam experiments.

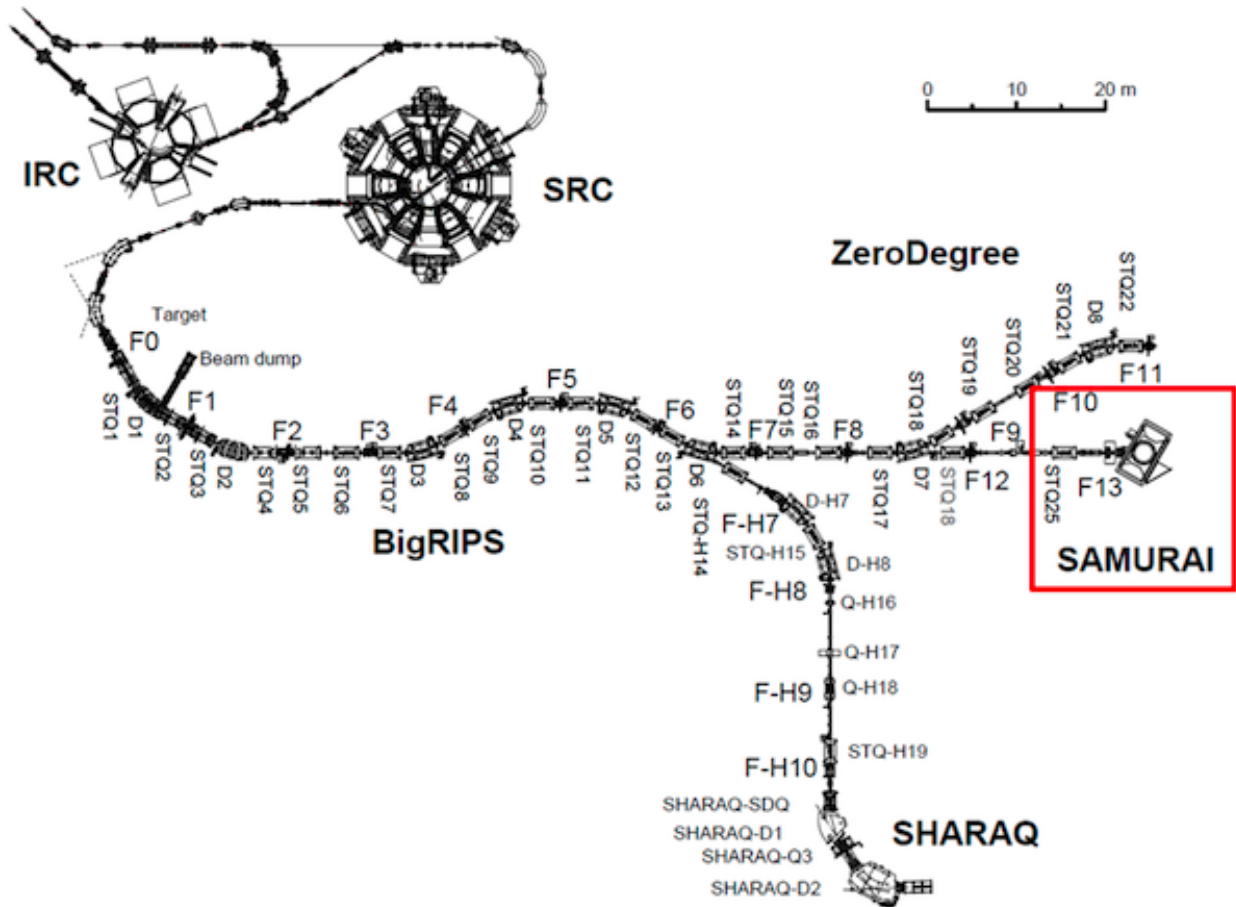


Figure 3.4: Overview of the RIBF, BigRIPS, and SAMURAI beamline.

3.5 Experimental Setup

3.6 Trigger Condition

How it was made using kyoto krakow

3.7 Collision Data Taken

CHAPTER 4

DATA ANALYSIS I: CALIBRATION AND CORRECTIONS

Need to explain pedestal subtraction GG noise subtraction

4.1 Software

The $S\pi$ RITROOT software is modular tasked based code based on the FAIRROOT package written in C++ [4]. The main tasks in the $S\pi$ RITROOT software reconstruction are:

- Decoder task
- Pulse Shape Algorithm (PSA Task)
- Helix Track Finding Algorithm
- Clustering Algorithm
- Track Fitting (GENFIT package)
- Vertex Fitting (RAVE package)

The decoder task converts the binary data file into a container class which maps the electronics channels into the corresponding pads and (x,z) coordinates.

There may be several pulses in a pad coming from two tracks passing under the same pad separated by arrival time. Using an expected pulse shape the PSA task fits the signal pulses within a pad, giving the arrival time of the drifted electrons from each particular track. The height of the fitted pulse is proportional to the total charge of that event, Q and the y -coordinate is calculated as $y = v \cdot t_0$ where v is the drift velocity and t_0 the arrival time. Combining the information from these first two tasks, (x,y,z,Q) , we construct what is called a "hit".

The Helix Track Finding Algorithm finds the collection of hits belonging to one track out of all the hits in an event. The hits within a track are then reduced into clusters. A cluster's position is

the average position of the hits within a cluster, with the total charge of the cluster being the sum of the hits charges.

A tracks average position is estimated by the cluster's average position. The clusters are then fitted in the GENFIT track fitting package [5], giving the final momentum of the track. A final vertex of the event is fitted from all tracks using the package RAVE [6].

Definition of clustering A brief description of the method of clustering is illustrated in Figure 4.1. It is impractical to cluster in both the x and z-axis and we only cluster the hits along one axis. The three clusters at the bottom of Figure 4.1 are clustered along the x-axis and the upper three are along the z-axis, as shown by the bolded pads for one of the clusters in each direction.

The clustering direction depends on the angle of the track with respects to the x-axis, defined as θ . For example, a track going along the z-axis the crossing angle is defined as 90° , and a track going along the x-axis defined as 0° . In the case that the crossing angle is $45^\circ < \theta \leq 90^\circ$ the clustering direction is along the x-axis. For $0^\circ < \theta \leq 45^\circ$ it is along the z-axis.

The position along the clustering direction is calculated by weighting the individual hit's positions by their charges q_i and getting the mean value. The other direction is set to the center of the pad. For example if we are clustering along the x-axis for a cluster, the z-position is set to the center of the pad in the z-direction and vice versa.

Clustering in this way gives us better position resolution for calculating the position of each cluster. You could imagine if we calculated the clusters only along the x-axis for tracks with $\theta \approx 0^\circ$ the x-position is not well defined. By clustering in the direction most perpendicular to the track, we get a better position resolution.

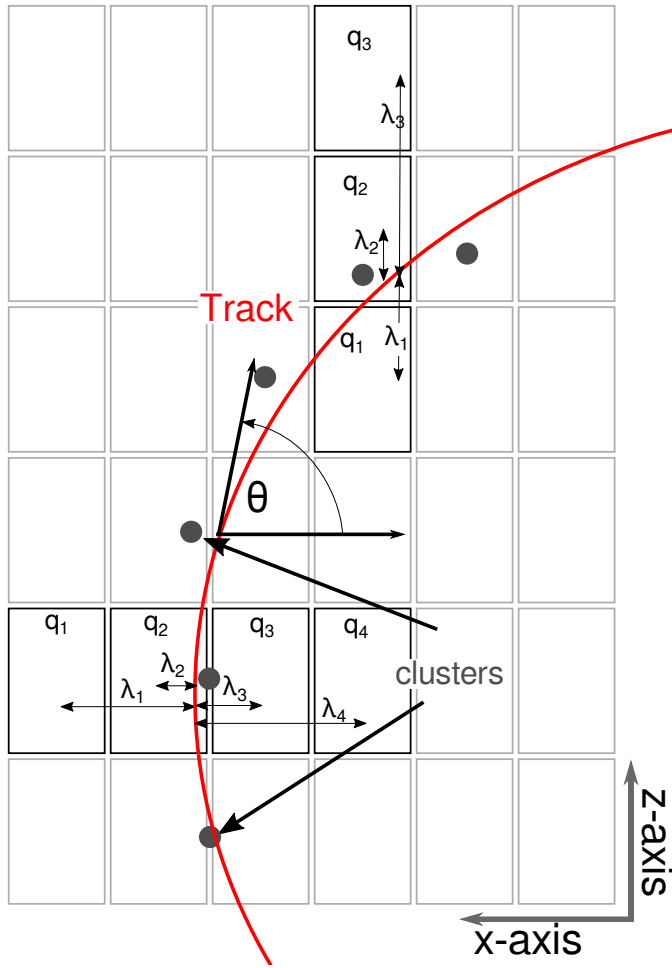


Figure 4.1: Cartoon graphic of a top down view of a fit to a track passing through several pads. The bolded pads and the charges q_i represent the hits belonging to that pad and the clusters of the track representing the average position of the track. The three clusters at the bottom are clustered in the x-direction and for the upper three clustered in the z-direction. The estimate of the position of the avalanche is given by the track fit and the position from the center to each pad to the \bar{x} position is given as λ_i .

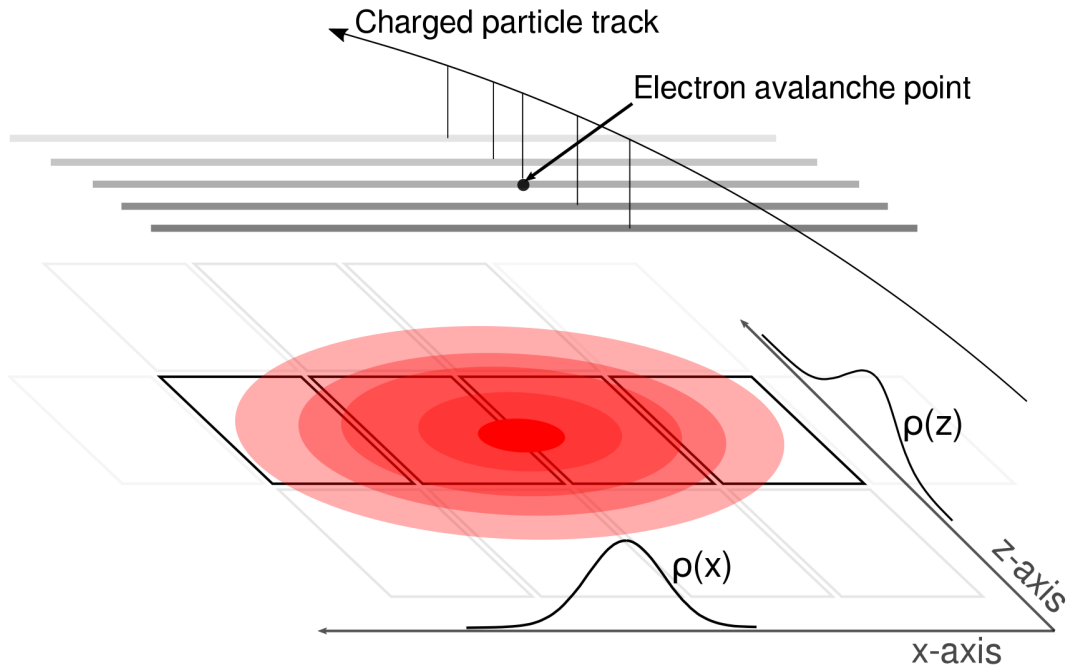


Figure 4.2: A cartoon illustration of the charge distribution resulting from an electron avalanche on one wire and the projections of the distribution onto the two axis $\rho(x)$ onto the x-axis and $\rho(z)$ onto the z-axis. The orientation of the wire planes is flipped upside down to display the perspective better.

4.2 Calibrations and Corrections

4.2.1 Cocktail calibration

Cocktail Calibration Picture of cocktail before and after ExB effect Table of LISE++ expected cocktail energies rigidity setting of dipole magnets (reference big rips line)

4.2.2 Electronics calibration

Pulse the ground grid.

Particle	100MeV			100MeV			300MeV		
	Measured			Measured			Measured		
	Raw	E×B							
p	882.8	929.5	877.3	903.5	929.5	889		f	f
d	817.1	d	d	898.5	e	e	1621.1	1704	1612
t	589.5	d	d	887	e	e	1612.4	f	f
³ He	1617.3	d	d	1795.2	e	e	3236.4	f	f
⁴ He	1405.6	d	d	1782.9	e	e	3226.4	f	f

Table 4.1: Summary of expected cocktail.

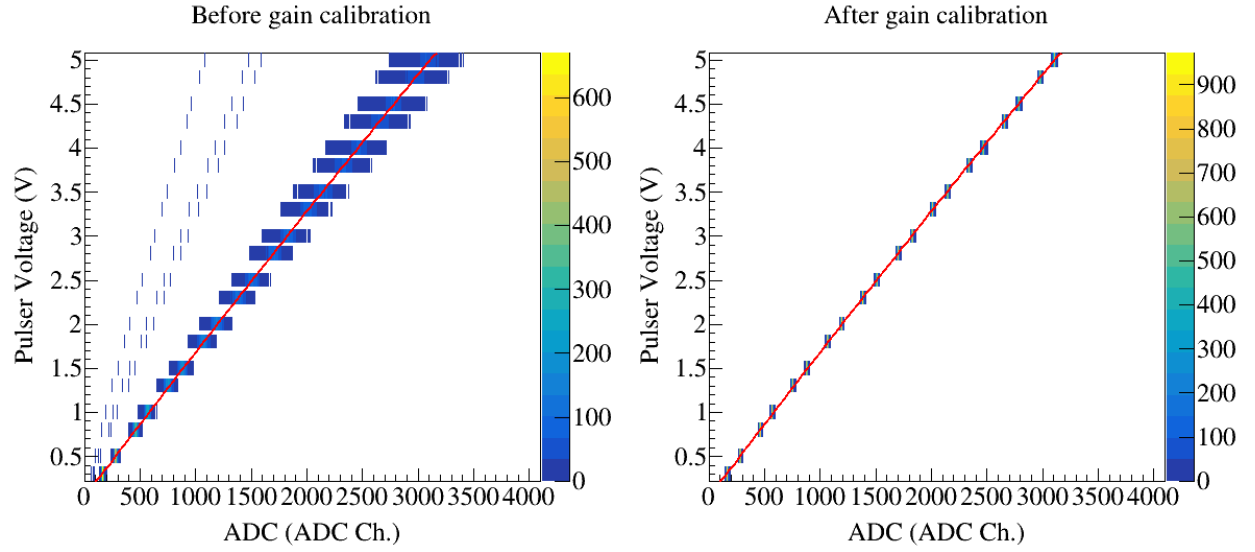


Figure 4.3: Calibration of electronics

4.2.3 Anode gain calibration

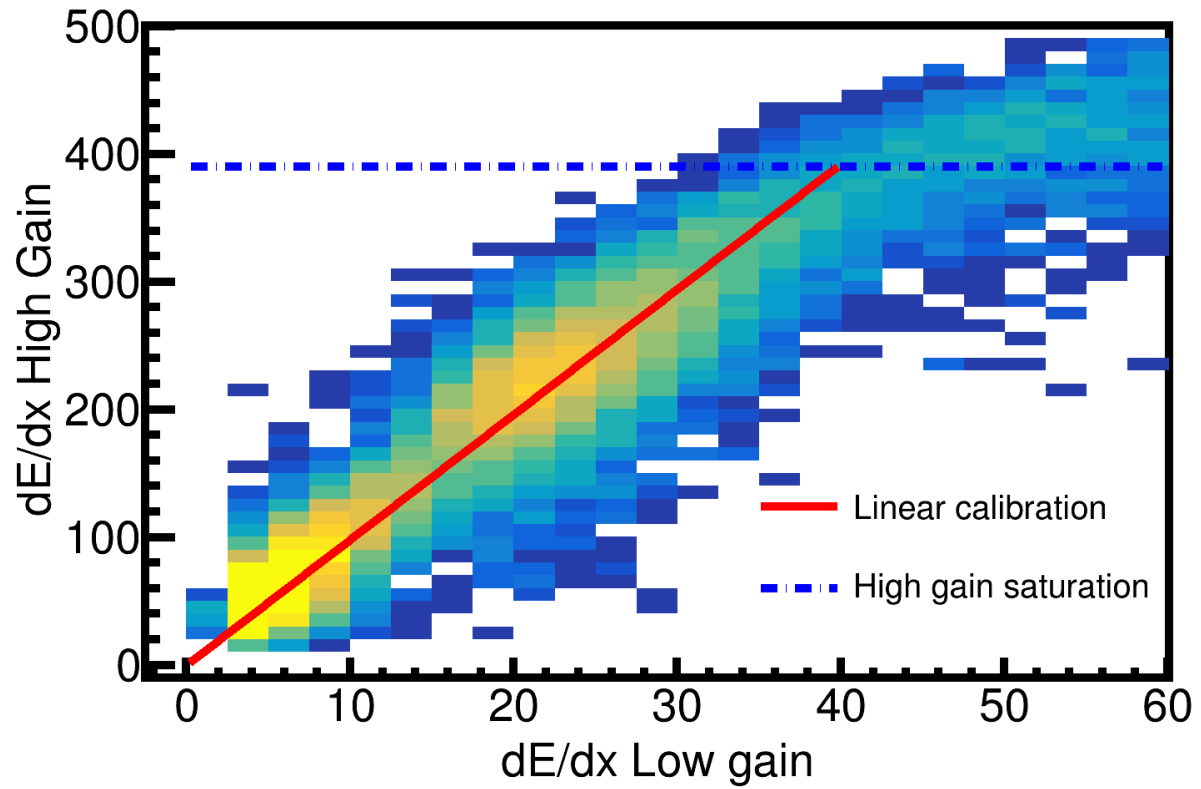


Figure 4.4: Calibration of low high.

Picture of low vs high gain channels and fit

4.2.4 Extending the dynamic range of the Electronics

Add paper here.

4.2.5 Space Charge Corrections

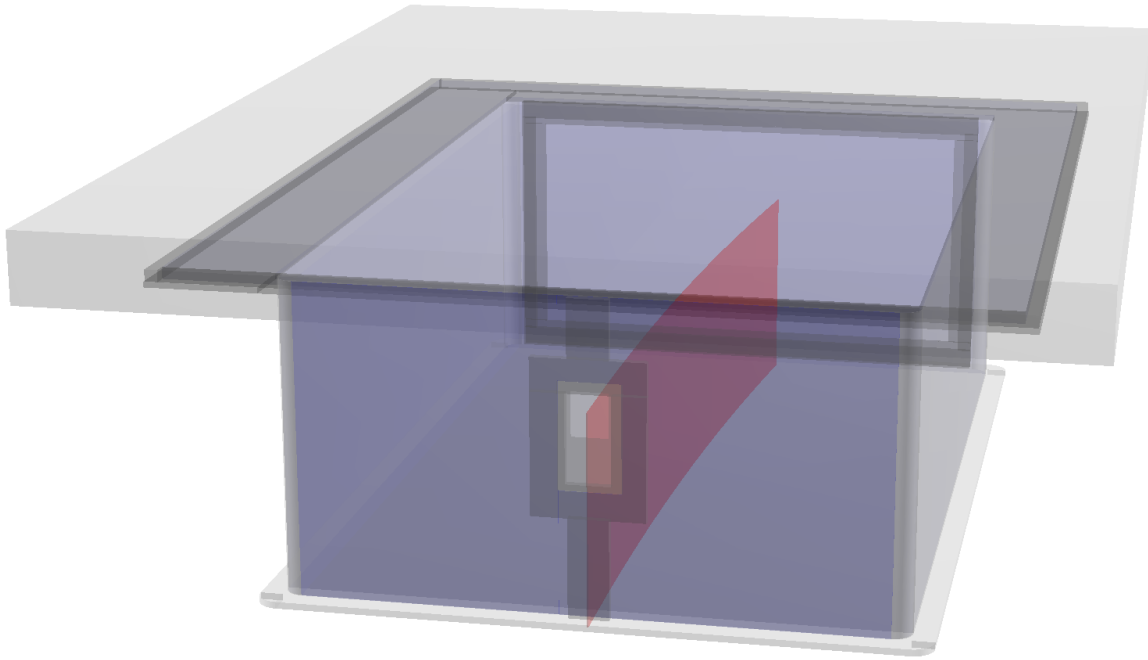


Figure 4.5: Location of space charge in ^{132}Sn

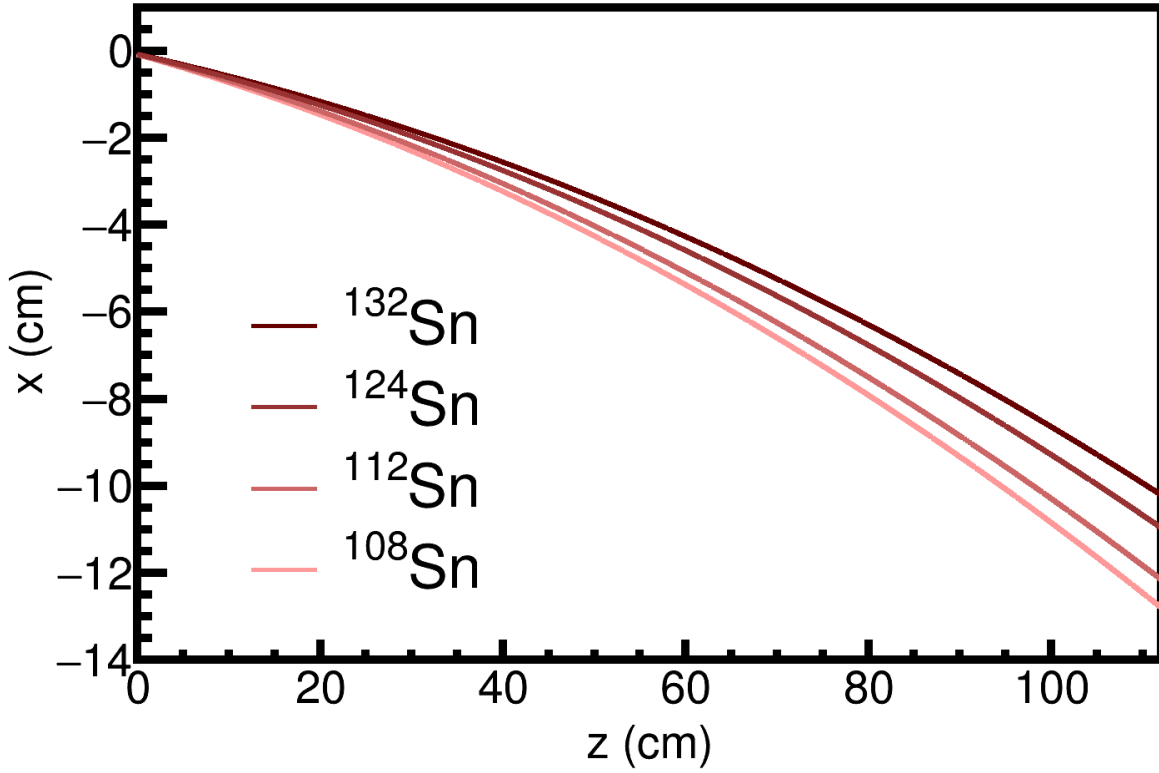


Figure 4.6: Beam path of the experiments

As the beam passes through the field cage it ionizes the gas along the way creating electron-ion pairs. The drift velocities of the ions are 1×10^4 times slower than the electron drift velocities. Because ions move very slow, the potential build up of positive ions may create a space charge which distorts the drifting electrons of the tracks, impacting the measurement of their momentum. There are several regions of the TPC in which electron-ion pairs are created. The largest source of positive ions are created in the avalanche process near the anode wires. These ions slowly drift toward the cathode and are captured by the gating grid. The other source of ions come from the primary ionization produced by the beam and reaction products in the detector gas. The energy loss $\langle dE/dx \rangle \propto Z^2$, where Z is the charge of the particle type. Because the charge of the un-reacted beam is around $Z 50$, the ionization due to the beam is a factor of 2.5×10^3 times that of the light charged particles which mostly are of charge $Z 1$. The beam is positioned about 25cm below the anode plane in the TPC. It takes electrons approximately 5 μ sec to drift to the anode plane. It takes

the ions $5 \times 10^4 \mu\text{sec}$ to travel. The beam rate in the experiment varied around a value of about 10kHz, which has an average occurrence of 1 beam every $100 \mu\text{sec}$, which is much shorter than the time it takes for the ions created by each beam to terminate on the cathode plane. This results in a build up of positive ions in the shape of a sheet charge, carved out by the beam path as shown in Fig. 4.7. The average distance between sequential ion paths created by each beam is a spacing of about $50 \mu\text{m}$ apart, and the average number of beam paths that compose the sheet charge is around 500 tracks. Though the arrival time of each beam track is random, the large number of tracks, and small inter beam spacing, allows us to approximate the sheet charge as an uniform sheet charge.

The electric field in the presence of the sheet charge can be calculated by solving Poisson's equation,

$$\nabla^2 \phi = \rho, \quad (4.1)$$

where ϕ is the electric potential and ρ is the free space charge; given the Dirichlet boundary conditions of the field cage. The electric field is given as the gradient of the potential, $\vec{E} = -\nabla \phi$.

To reduce computation time, we notice that $\vec{E} \propto \rho$, we can therefore solve the electric field for a reference free charge ρ_o and scale the solution for any other free charge. The full magnetic field map is provided by the SAMURAI collaboration [7]. The velocity field map is given by Eq. 3.1 and the electron drift through this velocity map is propagated by using a time stepped 4th-Order Runge-Kutta integration. The correction map is calculated by starting from the anode y-position and the measured (x,z) on the pad-plane and stepping backward in time in the Runge-Kutta integration through the velocity field map until the electron reaches the measured y-position.

It has been shown before that the amount of space charge present in the chamber is related to observables such as the distance of closest approach of each track to the vertex point [8]. This is easily understood, as the space charge distorts the electrons as they drift through the chamber eventually distorting the overall shape of the measured track. In the presence of no space charge, you would correctly expect the distance of closest approach of each track to the vertex point would

be a distribution centered around zero. In the presence of space charge the tracks are distorted and the distribution has some mean bias.

Shown in Fig. 4.10 is an example of the distortion map in the TPC for left-going tracks in blue, and right-going tracks in green, with the vectors of distortion magnified. The space charge affects left and right going tracks differently, with the right-going tracks going to higher momentum values and the left-going tracks going to lower momentum values. The inset figure of Fig. 4.10 shows the shift in the x-position distance to vertex for the displaced left-going track given by ΔV_x , with the opposite direction for right-going tracks. We are able to measure the amount of distortion the space charge creates by measuring the difference between the most probable values of the left-going and right-going tracks which we define as ΔV_{LR} .

Overview Discuss the relevant time scales, drift lengths, magnitudes, and locations of space charge

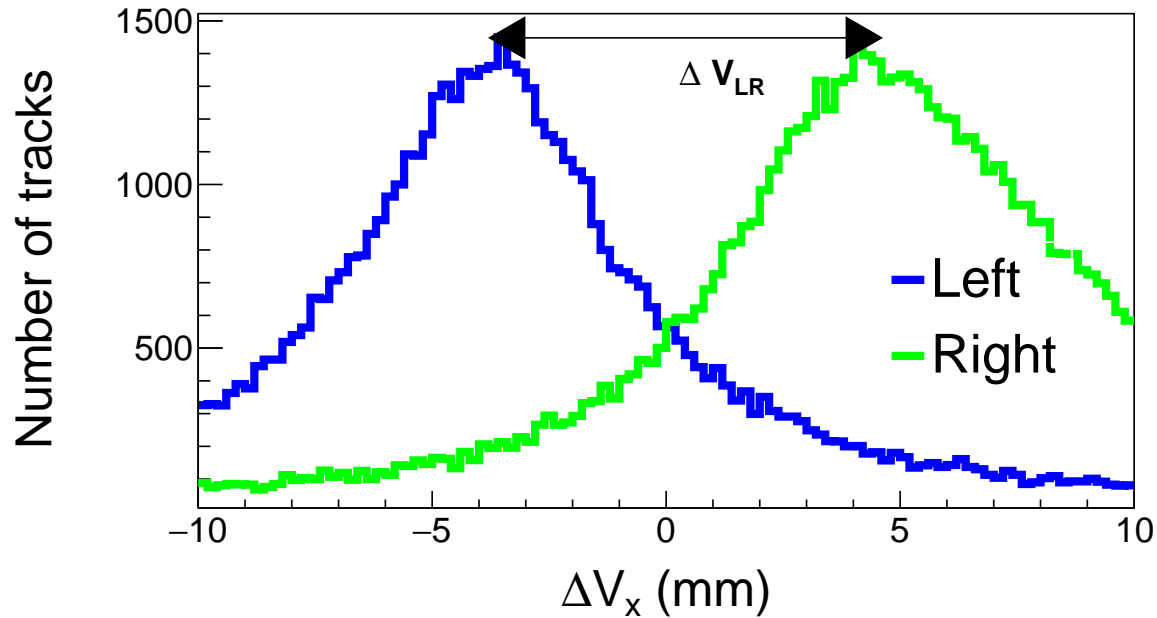


Figure 4.7: ΔV_x distribution for left-going and right-going tracks in the TPC for the

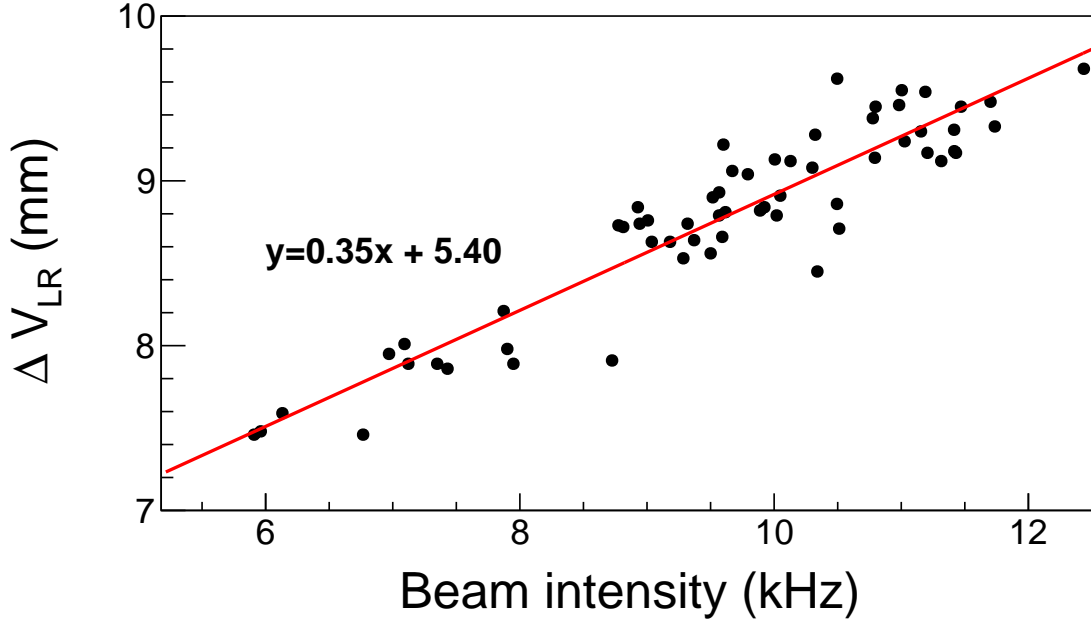


Figure 4.8: ΔV_{LR} as a function of the beam rate.

The average beam rate was recorded in each experimental run and slightly varied from run to run, due to beam production variations. The amount of space charge present in the field cage is directly proportional to the beam rate; therefore ΔV_{LR} is also proportional to the beam rate as shown in Fig. 4.8. The only parameter in the space charge correction algorithm is the surface charge density σ_{SC} . By varying σ_{SC} for a wide range of values the ΔV_{LR} observable is measured and plotted in the left panel of Fig. 4.9. The surface charge density which gives $\Delta V_{LR} = 0$ is taken to be the estimate for the average amount of space charge present. This is done for several runs which vary in beam intensity. Since the relation is linear between the surface charge density and the beam rate, a linear fit gives good agreement for interpolating the surface charge values as a function of beam rate, as seen in the right figure of Fig. 4.9.

This is done for all the systems. I NEED TO PUT THE ASSUMPTIONS OF 132 108 HERE!!!

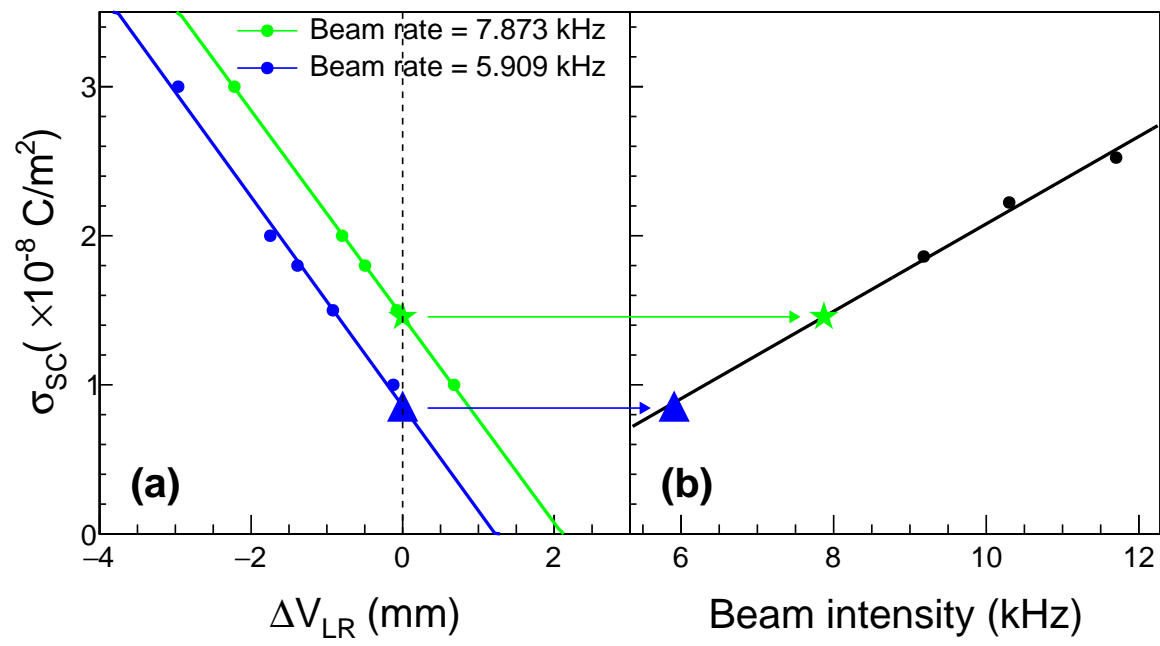


Figure 4.9: Space charge relation

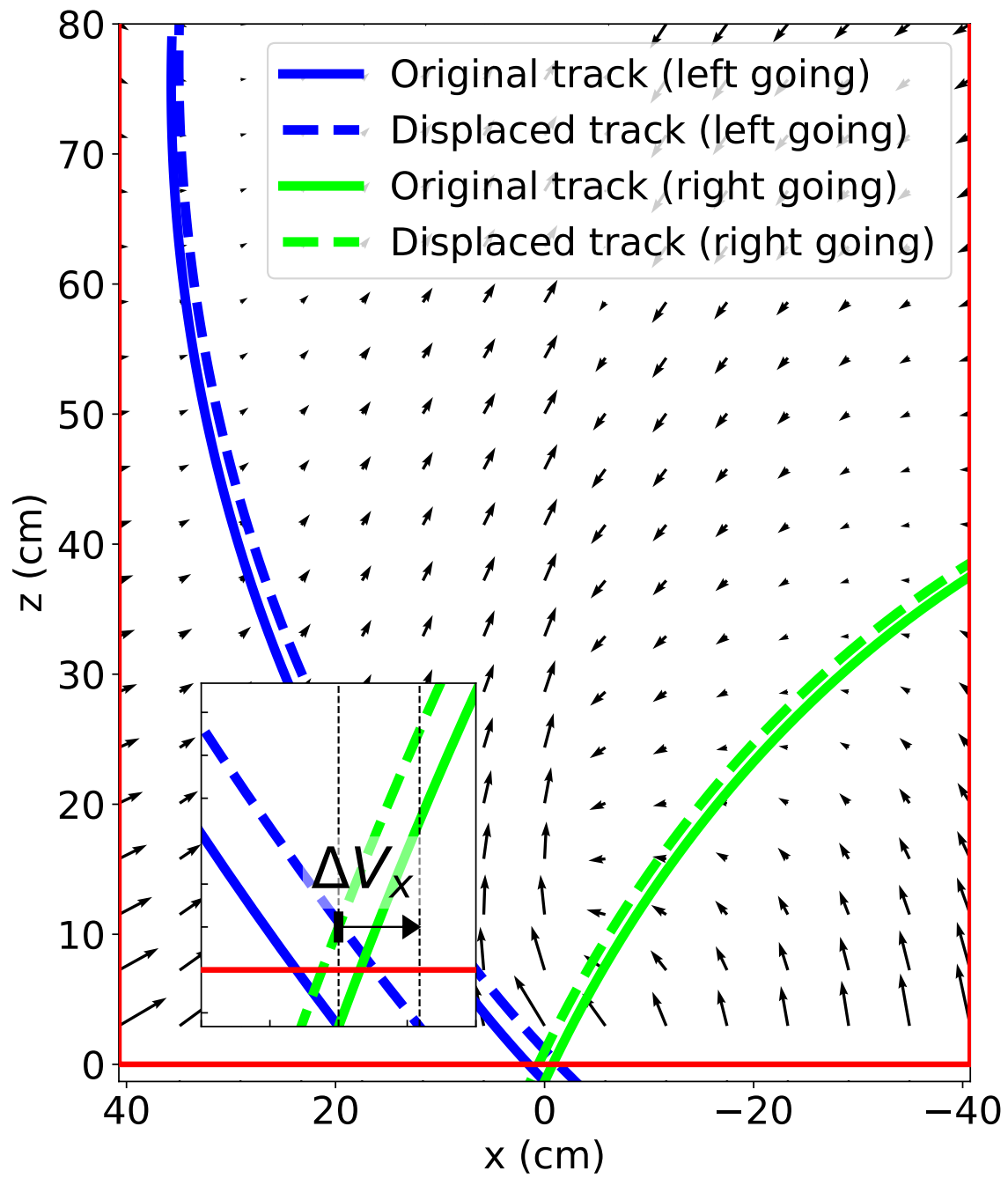
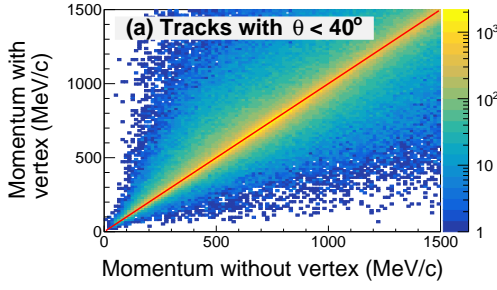
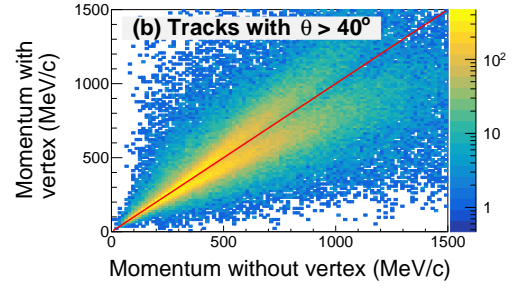


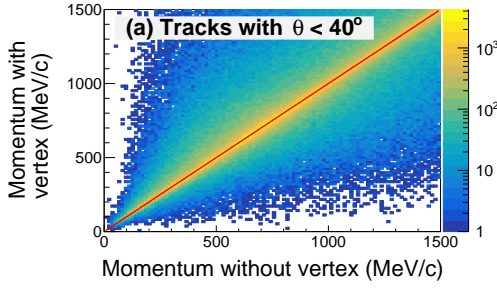
Figure 4.10: Shift of tracks



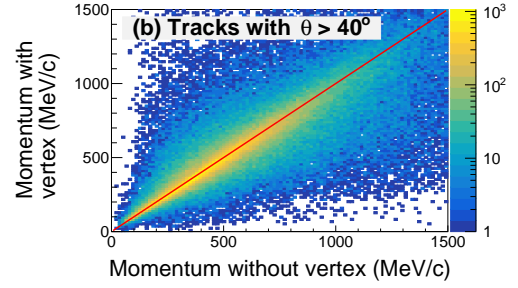
(a) Generic



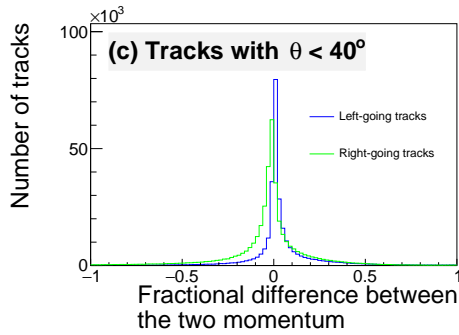
(b) Competitors



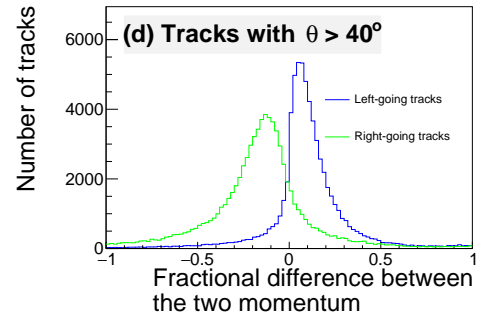
(c) Generic



(d) Competitors



(a) Generic



(b) Competitors

Beam Energy Loss	^{132}Sn	^{124}Sn	^{112}Sn	^{108}Sn	Avg.
keV cm^{-1}	11.2	0.034	5.43	903	150

Table 4.2: Average energy loss of each beam.

Reference appendix for poisson solver Tables for ion drift velocity in P-10 Gas reference Sauli
Figure of sDAC or POCA Figure of cartoon of what is happening to tracks Figure of correction
map in TPC and MC map Figure of before and after correction BDC vs reco momentum Figure of

track residuals before and after?

In theory, a TPC functions with the electric and magnetic fields parallel to each other. In this way the electrons move opposite to the electric field winding tightly around the magnetic field lines, reducing transverse diffusion in the process. In practice, due to the finite size of the dipole magnet and field cage, there are transverse components to both the electric and magnetic fields. These transverse components introduce drift velocities in the transverse directions, causing a shift in the measured cluster positions of the track. Thereby introducing systematic shifts in the calculation of the momentum and the vertex calculation.

Most of the time the beam does not undergo a nuclear collision with the target and passes through the TPC drift volume. The KATANA array threshold was set to veto such events, ensuring the gating grid remain closed to prevent the large amount of charge deposited by the beam into the avalanche region. While the electron drift velocity is fast enough for the electrons produced by the unreacted beam to terminate on the closed gating grid, the drift velocities of the positive ions produced are of order 10^{-4} times slower. At higher beam rates the positive charge is allowed to pile up producing a region of positive space charge, introducing perturbations to the nominal electric field.

Since the beam comes in along the z-axis, and the drift direction of the ions is in the -y direction, we can estimate the charge density as an uniform sheet charge. The surface charge density is related to the beam rate, ion drift length, ion drift velocity, and the energy loss of the beam. Though the incoming beam comes randomly, the slow drift velocity combined with the high beam rate makes the uniform approximation valid. Tracking or estimating the beam rate as a function of time within a given run would provide a better estimate of the space charge. Or experimentally a laser system could be pulsed after each event (throughout the drift volume), giving the experimental correction map for the drift. While the potential for a laser system was implemented in the field cage design, a laser system ultimately was not developed for the S π RIT tpc.

The beam rate within a run is roughly constant, therefore we can estimate the space charge and provide a first order correction for the space charge effect.

As mentioned in CHAPTER ??, the cocktail beam momentum was well known to within 1% as set by the BIGRips spectrometer. Also time of flight analysis of upstream and downstream scintillators also independently confirmed the beam rigidity setting. The expected momentum is given in TABLE ?? as calculated by from the beam rigidity setting of the magnet (WHICH MAGNET). The measured momenta as determined by the TPC software (given in FIG TABLE), shows a disagreement on the level of 5% too high. We noticed that if one only uses the first 90 layers (out of 112) of the TPC, the momenta is lower; one should expect the momentum to go higher as the track length is shorter (short tracks effectively are straight lines). In the cocktail beam there is no un-reacted beam causing any significant space charge. The magnetic field map of the SAMURAI magnet has been calculated by TOSCA simulation CITE ??, and several points have been verified experimentally with a hall probe to be within XXX %. We assume that the electric field (to first order) is uniform in the y-direction. Using Garfield++ CITE ??, we can model the transverse drift of the electrons in the presence of such fields.

A grid of electrons uniformly distributed in the TPC model space were drifted to the gating grid position. The final shifts in the x and z positions was measured.

4.3 Monte Carlo Simulation

We use Geant4 as and event generator for performing Monte Carlo Simulations in the TPC. A scale model of field cage, front window, front window frame, pad plane, and aluminum top plate are modeled. The correct materials are used as well as the field cage is modeled with P-10 gas at a density of ?????. By using Geant4 we can also input the the magnetic field map of the SAMURAI dipole magnet (as calculated by the SAMURAI group via a TOSCA simulation). In this way any particle type may be studied and the full interactions (scattering, decay, energy loss, path taken, etc.), are accounted for. The output of this simulation is a series of energy loss points which contain the amount of energy lost in keV/cm and the position in (x, y, z) .

Separate software tasks model the converting energy loss into electrons, the drifting of electrons,



Figure 4.13: A summary of all the effects modeled in the TPC MC simulation.

the avalanche process, and the electronics response.

4.3.1 Drift Task

The drift task takes the energy loss points calculated from Geant4 and converts them into electrons, and then modeling their drift behavior in the field cage. As discussed previously the various processes [CITE To formula about drifting electronc]

A full microscopic treatment of the stochastic nature of each electron would be too cumbersome; most of the properties of the electrons are described by macroscopic quantities can be described by The charge of each MC point is converted to the total number of electrons liberated in the P-10 gas. This is a well understood property of proportional counters and is stable over a wide range of velocities and particle types [CITE BOOK]. The conversion factor of P-10 can be calculated by considering the partial volumes of each component of the gas. 4.2.

$$Number of e^- = 28 keV/cm \quad (4.2)$$

4.3.2 Pad Response Task

After the avalanche process of the previous task, the total charge of the event is split over several pads defined by the Pad Response Function (as discussed in section ???). As shown in Fig. 4.14,



Figure 4.14: A cartoon of the wires over one pad.

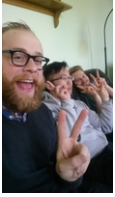


Figure 4.15: Comparison of MC and data PRF

there are three wires that lie directly above a given pad. The z coordinate of the avalanche can only be one of these three wires, where as the x coordinate can be any value along the wire. The functional form of the software PRF (given in Eq. 4.3), was tuned to match the experimental data. Shown in Fig. 4.15, we see the tuned software PRF can match the experimental PRF from data over several crossing angles (as mentioned in Chapter ??? governs the shape of the PRF).

$$PRF(x, z) = \frac{1}{2\pi\sigma_z\sigma_x} \exp \frac{-(x-x_0)^2}{2\sigma_x^2} \exp \frac{-(z-z_0)^2}{2\sigma_z^2} \quad (4.3)$$

4.3.3 Electronics Task

The electronics task takes the total charge on each pad and simulates the electronics response, converting electronics into ADC channels. Accounting for the pedestal, the measured output in ADC channels (for a given gain setting) is given in Eq. 4.4.

$$1_{\text{ADC}} = \frac{ADC_{\text{Max}} - ADC_{\text{Pedestal}}}{G * f_c} \quad (4.4)$$

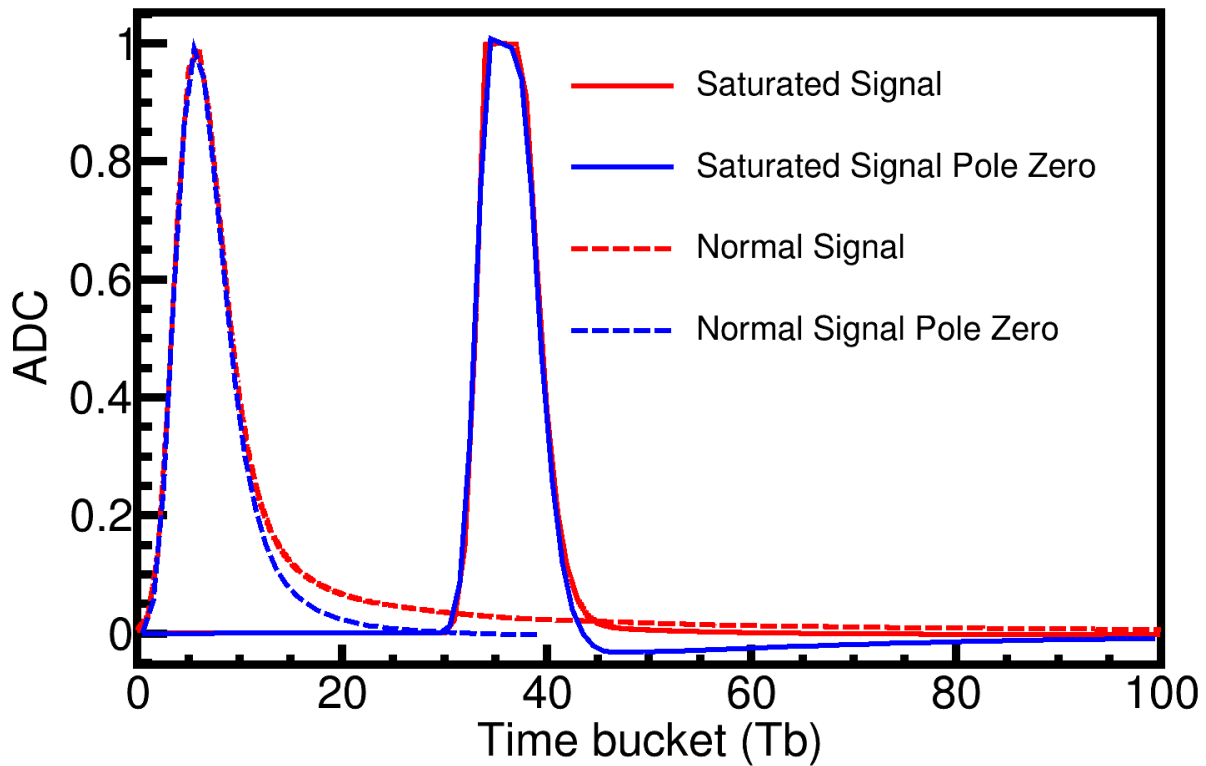


Figure 4.16: Pulse shapes for normal and saturated signals. Both are normalized to a max height of 1.

4.3.4 Simulating Saturation

Add figure showing saturated time bucket spectra with location of saturation identified and with pulse shape from embedding I would like to add and how it blocks it. Add Figure with 2D pad plane response with and without saturation flag

4.4 Monte Carlo Track Embedding

Add Figure of MC track embedding

Track embedding is the process of taking a simulated MC track from Geant4 and embedding its response into a real data event. After reconstructing this new embedded event we match the input MC track embedded to its corresponding final reconstructed track. By doing so we can evaluate the response of the entire TPC system to any given input value. The TPC system is composed of

three major components (each which can introduce errors and or biases) the software, the detector, and the experimental setup.

As discussed in [SOFTWARE CHAPTER] the software is composed of several task, each which introduce some error. Table REF TABLE] listing some of the errors each task may introduce illustrating how difficult propagating the errors would be through each system.

The detector system itself introduces errors related to the physical processes of the measurement itself. To address this we model the TPC (and its materials) in a Geant4 simulation which provides an accurate description of various interactions of a particle traversing the materials (including the gas volume) of the TPC.

software is the most straight forward; let the software routine process an input and measure the result. Understanding the measurement requires modeling the physics involved in the theory and operations of TPC's and the electronics. The experimental setup itself is quite large and complex, several ancillary detectors such as the Kyoto multiplicity array, Krakow veto array, Active veto array, beam identification detectors, etc. Even if a full accurate model could be constructed the complex trigger logic of the DAQ system would be impossible to model. If we notice that the biases and errors of the entire experimental setup is contained in the measured experimental data. Therefore, by inputting the MC data into a real experimental event (and measuring the output of that MC track) we can estimate the errors of the experimental setup.

The software analysis routine and the bias introduced by the trigger settings of the experiment introduce systematic errors in the reconstruction of tracks

4.4.1 MC and Data Comparison

Add Figure of Pad response function for pion,proton.... for MC vs Data vs angles... Add Figure of Number of clusters of MC vs Data Add Figure of dEdx MC vs Data Add Figure of Momentum resolution MC vs Data Add Figure of track residuals? MC vs data?

4.5 Efficiency Corrections

Add Figures of efficiency vs angles in TPC polar angle plot for pions

Since the $S\pi$ RIT TPC is a fixed target experiment it's angular coverage is certainly not 4π . Because the target is several cm away from the widow of the field cage the geometric acceptance is not even 2π . The rectangular design complicates the calculation of the geometric acceptance, or the efficiency.

4.6 Beam Particle Identification

Figures of beam contaminants in our beam PID line. Table of beam purity reference to Jon's thesis paper

4.7 Solid angle coverage

APPENDIX

APPENDIX
YOUR APPENDIX

BIBLIOGRAPHY

BIBLIOGRAPHY

- [1] Y. Yano, The ri beam factory project: A status report, Nucl. Instrum. Meth. B 261 (1-2) (2007) 1009–1013. doi:10.1016/j.nimb.2007.04.174.
- [2] T. Kobayashi, et al., Samurai spectrometer for ri beam experiments, Nucl. Instrum. Meth. B 317 (2013) 294–304. doi:10.1016/j.nimb.2013.05.089.
- [3] E. Pollacco, et al., Get: A generic and comprehensive electronics system for nuclear physics experiments, Physics Procedia 37 (2012) 1799–1804. doi:10.1016/j.phpro.2012.02.506.
- [4] M. Al-Turany, et al., The fairroot framework, J. Phys.: Conf. Ser. 396 (2). doi:10.1088/1742-6596/396/2/022001.
- [5] C. Höppner, et al., A novel generic framework for track fitting in complex detector systems, Nucl. Instrum. Meth. A 620 (2-3) (2010) 518–525. doi:10.1016/j.nima.2010.03.136.
- [6] W. Waltenberger, Rave—a detector-independent toolkit to reconstruct vertices, IEEE Transactions on Nuclear Science 58 (2) (2011) 434–444. doi:10.1109/TNS.2011.2119492.
- [7] S. Collaboraiton, Samurai dipole magnet field map (2020).
URL <https://ribf.riken.jp/SAMURAI/index.php?Magnet>
- [8] G. Van Buren, et al., Correcting for distortions due to ionization in the star tpc, Nucl. Instrum. Meth. A 566 (1) (2006) 22–25. doi:10.1016/j.nima.2006.05.131.